DOI: 10.13009/EUCASS2022-6165
9TH EUROPEAN CONFERENCE FOR AERONAUTICS AND SPACE SCIENCES (EUCASS)

Review and Implementation of Engineering Models of Rocket Film Cooling and Nozzle Erosion

Simone D'Alessandro⋆*, Pierluigi Concio, Marco Rotondi, Daniele Bianchi and Francesco Nasuti*
Sapienza University of Rome
Via Eudossiana 18, 00184, Rome, Italy
⋆Corresponding author

Abstract

The present work, reviews the improvements which have been implemented in the European Space Propulsion System Simulation (ESPSS) libraries v3.6, regarding the chamber film cooling and the nozzle erosion. In particular, attention is focused on the adopted mathematical modeling of the phenomenology, on models implementation into the ESPSS libraries, and lastly on the validation procedure.

Active chamber cooling and nozzle erosion are two important and common design choices regarding liquid and solid/hybrid rocket engines, respectively. Dealing with liquid engines, active cooling systems are often required to extract heat from the hot-gas flow and specifically, the film cooling represents a valid design solution in support of the regenerative cooling system, capable of providing a significant protection to the chamber at the cost of a performance loss. On the other hand, the use o an ablative thermal protection system (TPS) represents a widespread solution to protect the nozzle structure from the chamber harsh thermochemical environment if other kind of cooling techniques are not feasible, as in the case of solid and hybrid rockets. As a drawback, ablative materials are subjected to a thermochemical erosion process, leading to a nozzle throat enlargement and thus to a specific impulse loss and to a modified thrust curve.

During the design process, reliable numerical models are necessary to reduce the number of expensive hot-firing tests. In this sense, the European Space Propulsion System Simulation (ESPSS) framework has been historically conceived developed by ESA to simulate complex systems steady-state and transient analyses.

The inclusion of film cooling and nozzle erosion low-order models might represent an useful asset during the engine development phase, allowing for quick evaluations of complex phenomena in an inter-dependent system-wide representation. Reliability of the results is assessed by comparing the numerical results with experimental test cases and CFD simulations.

1. Introduction

Film cooling is a cooling method used in liquid rocket engines (LRE) to protect combustion chamber and nozzle walls against high thermal loads. A controlled flow of coolant is introduced either in liquid or gaseous phase as a thin film through slots or discrete holes, placed in the combustion chamber, either at the outer row of the injection faceplate or at different positions downstream towards the nozzle. Such injection lowers the mixing efficiency locally, yielding to performance losses. For that reasons the amount of film coolant mass flow rate has to be limited. Film cooling might represent an interesting choice, used in synergy with the regenerative cooling technique, especially when dealing with high pressure engines, characterized by high thermal loads.

Concerning Liquid Film Cooling (LFC), three challenging aspects can be defined, i.e the liquid film stability, its evaporation rate, and thus the extension of the liquid phase at the wall, called Film Cooled Length (FCL).

The determination of the evaporation rate for both inert and reactive coolants was the subject of different early analytical and empirical studies [1, 2], employing lots of assumptions to obtain results in closed form, and hence yielding to a very limited applicability range, in some cases [3, 4]. Different attempts have been made to develop correlations accounting also for the entrainment of liquid droplets in the gaseous phase [5, 6]. Even nowadays, the liquid entrainment and film stability phenomena are still an open problem [7], and there is a lack of experimental information in rocket-like conditions.

Different semi-analytical, 1-D differential and 0-D algebraic formulations have been developed, including also the liquid entrainment and hot gas radiation modeling, for the calculation of FCL and the evaporation rate [8–10], with a fairly good agreement, especially concerning the last two.

DOI: 10.13009/EUCASS2022-6165

Concerning Gaseous Film Cooling (GFC) investigations, they were dedicated to understand the effects of different coolant injection procedures [11], free stream turbulence level [12], and compressibility [13] of the main stream boundary layer. It was found that no significant changes of cooling performance occur because of variations in the turbulence intensity of the coolant jet. Gas compressibility is found to change the growth rate of the shear layer between the main and secondary flow. The determination of GFC performance has been mostly carried out empirically. A great number of studies and results is available in open literature concerning gaseous film cooling, but, unfortunately, only few recent numerical analyses have been carried out aiming to study of rocket thrust chambers [14–18]. Significant improvements have been made [15–18], proposing further dependencies and modelling of phenomena occurring in rocket combustion chambers.

Nozzle erosion is a phenomenon in which nozzle surface recedes because of the chemical and mechanical interaction with the hot gases, increasing the nozzle throat area and resulting in a performance loss. Carbon-based ablative materials are commonly used in nozzles of solid rocket motors (SRM) and hybrid rocket engines (HRE) as thermal protection systems (TPS) because of their good thermal and physical properties. The description and modeling of the major physical mechanisms governing the erosion and the thermo-physical behavior of the TPS are therefore of fundamental importance.

In the open literature, different high-fidelity numerical approaches to the nozzle erosion problem can be retrieved, ranging from ablative one-dimensional and multi-dimensional material response solvers [19–21] to finite-rate ablative boundary conditions and gas-surface interaction (GSI) models integrated in Computational Fluid Dynamics (CFD) solvers [22–34]. However, few low order representation of the nozzle erosion phenomenon, such as analytical or semi-empirical models, are currently available. As mentioned dealing with the film cooling, a low order representation of a complex phenomenology such as the nozzle ablation problem might represents a useful tool during the engine design phase.

The simplest approaches to the nozzle erosion problem are represented by analytical and semi-empirical models. The literature contains relatively few exact analytical solutions of the heat conduction equation in which phase changes and the associated latent heat are considered. In the 60s, Baer and Ambrosio [35] dealt with this problem. However, the analytical solutions proposed in [35] have a limitation in the possibility to handle only constant recession rates and/or constant incoming heat fluxes. Semi-empirical correlations for SRM [36, 37] and HRE [38, 39] nozzle throat erosion are instead able to take into account the main functional dependencies of the ablation phenomenon, such as propellant composition and chamber pressure. However, they are limited to few specific propellant combinations, and cannot be generalized.

In the 60s, the thermochemical response solver Charring Material Ablation (CMA) [19] has been developed. It is based on the so called equilibrium B' tables model which has been the reference NASA ablative code until the late 90s. The B' tables employed in the CMA numerically represent a general ablation function for a specific TPS material and a specific boundary-layer edge gas. The CMA model relies on a heat and mass transfer coefficient formulation [40, 41], hence simplifying assumptions are necessarily needed, including semi-empirical correlations to take into account geometrical and/or chemical side effects (e.g., nozzle throat radius and blowing). Moreover, the B' tables are usually computed assuming chemical equilibrium between the solid material surface and the external boundary-layer edge gas, which is a reasonable assumption only in the diffusion-limited ablation regime (i.e., extremely fast surface reactions) [25]. Hence, such approach cannot be employed in case of kinetic-limited ablation regimes, such as for most HRE [29].

Recently, an interesting simplified ablation model, able to take into account surface chemistry phenomena including finite-rate effects, has been proposed in [42]. The method has been developed for a propulsive system analysis code used for SRM preliminary design, hence fully based on reduced models. However, the main limitation of the proposed methodology is the lack in prediction of the boundary layer effects on chemistry, leading to possible reliable results only in case of strongly kinetic-limited ablation regimes.

The EcosimPro/ESPSS framework allows to assemble and simulate complete propulsion systems by connecting the individual components available in the software libraries to each other [43]. Furthermore, it allows to design and develop brand-new components to be included in the models, in turn. In such a friendly environment, the user can have a quick assessment of a complete rocket engine, even if in an approximate fashion.

In this context, the present work aims to improve the ESPSS libraries capabilities by adding two new components to their pool, namely liquid- and gaseous film cooled LRE thrust chambers, and by improving the available solid and hybrid thrust chambers adding nozzle erosion prediction capabilities. Three models for LFC and one for GFC have been included in the new liquid thrust chambers, while two erosion models have been implemented for each of solid and hybrid thrust chambers.

DOI: 10.13009/EUCASS2022-6165

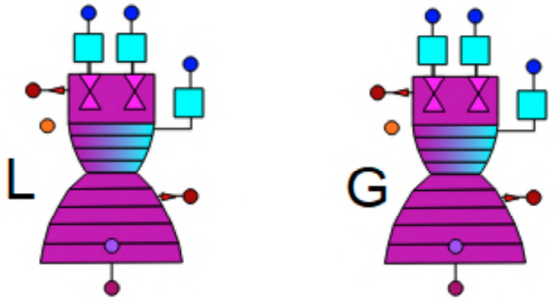

Figure 1: New liquid (L) and gaseous (G) film cooled thrust chamber components.

Validation is then carried out by comparing the results with experimental data available in the literature, and with CFD simulations both purposely carried out and taken from the literature.

2. Numerical models

In the present section, the implemented models are presented, as well as their implementation strategy in the ESPSS libraries are presented, for both chamber film cooling and nozzle erosion.

2.1 Film cooling

As mentioned, the LFC and GFC models have been implemented in two brand new components, which inherit the features of the "CombustChamberNozzle" existing component, including the film cooling interactions with the heat exchange and with the hot flow, depending on the models assumptions. The components are shown in Figure 1. The motivation for separating the liquid from the gaseous cooled components lies in the fact that the added models are quite invasive, yet significantly different from each other.

The implemented formulation aims at predicting the main features of a film-cooled combustion chamber, namely,

1. the film extension before complete mixing/entrainment occurs (in case of gaseous/liquid coolant, respectively),
2. the effective reduction of wall heat flux in the cooled region,
3. the O/F ratio shift resulting from film addition and its effect on performance, while retaining reasonable computational times.

Concerning liquid film cooling, the model uses the hot-gas flow thermodynamic state and properties as inputs (in compliance with the model requirements) to compute a fixed set of quantities, i.e., evaporation rate, heat fluxes, boundary layer mass flow rate and temperature, which are calculated at each time step, according to the chosen model features. Film injection can take place at any chamber node. The hot gases and the coolant are considered as two separate entities, ruled by their own conservation laws, interacting with each other due to the coolant evaporation. Such dynamics has been included in each of the coolant and hot flow conservation laws as a distributed mass flow rate source term, along the chamber. Such modeling allows for

1. chamber pressure increases due to the distributed mass flow rate injection, due to the coolant evaporation;
2. chamber temperature and O/F ratio variation due to the coolant enthalpy and species mass fraction addition;
3. hot gas flow heat loss increase, due to the heat transferred to the film flow.

It has to be remarked that the computations of the coolant evaporation and of the thermo-chemical state of the hot stream are interdependent, and for such a reason, an iterative procedure is necessary.

Concerning gaseous film cooling, the logic is similar except for the evaporation process, which is not present. Hot gases, film, and the mixing fan regions are treated independently, each of the three ruled by their own conservation laws, with appropriate interaction source terms. The different regions are then combined to extract the correct wall heat load distribution. Due to the typically low coolant mass flow rates in this case, the thermo-chemical influence of the coolant stream on the hot gas flow is neglected.

Because of the nature of the ESPSS framework, different kind of models have been selected from the literature, capable of delivering different orders of accuracy while requiring different levels of computational efforts.

DOI: 10.13009/EUCASS2022-6165

2.1.1 Grisson model for LFC

Grisson model [9] is a one-dimensional differential model for liquid film cooling in liquid rocket engine combustion chambers. The main model features include the calculation of the coolant evaporation rate due to heating and, as a consequence, the estimation of the length of the liquid phase-film cooled region. Convective and radiative heating of the film are considered. Liquid droplets entrainment into the hot gas stream is neglected in this model, thus its application to reduced coolant mass flow rate test cases is recommended. Even after that the cooling stream completely evaporates, Grisson's model assumes that the coolant keeps flowing in the vicinity of the walls, providing an additional vapor phase protection, downstream.

By model, as long as the liquid phase is present at the walls, the convective heat flux coming from the hot gases is completely absorbed by the film stream, while the streams provides convection to the walls. Convection from the hot flow to the cold stream is corrected to consider the film transpiration. Radiative heat on the other hand, is partially absorbed by the film stream, and partially transferred to the walls. After the liquid phase is completely evaporated, both convective and radiative heat flux reach the walls, in a model-corrected way.

The evaporation rate is iteratively calculated as follows

$$\dot{m}_{vap} = \frac{\dot{Q}_{\text{conv,film}} + \dot{Q}_{\text{rad,film}} + \dot{Q}^{\text{wall}}_{\text{conv,film}}}{\lambda} \tag{1}$$

$$\frac{h}{h_0} = \frac{\log\left(1+H\right)}{H} \tag{2}$$

$$H = \frac{K_m\, c_{p,g}}{\lambda}\left[\left(T_g - T_{sat}\right) + \frac{\dot{Q}_{\text{rad,film}}}{h}\right] = \frac{K_m\, c_{p,g}\, \dot{m}_{vap}}{h} \tag{3}$$

where $\dot{m}_{vap}$ is the evaporation rate, $Q_{\text{conv,film}}$ and $Q_{\text{rad,film}}$ are the convective ad radiative heat fluxes entering the liquid film, λ is the latent heat of vaporization, h_0 and h are the hot side regular and transpiration-corrected convective heat transfer coefficients, $c_{p,g}$ is the hot gas specific heat at constant pressure, K_m is a correction factor depending on hot gas and film molar masses, T_g is the hot gas temperature, and T_{sat} is the liquid film saturation temperature.

The Film Cooled Length (FCL) is determined as the abscissa at which the coolant mass flow rate is totally consumed.

2.1.2 Simplified Grisson model for LFC

Grisson [9] also provided a simplified 0-D analytical formulation of his model to avoid the iterative calculation of the evaporation rate and the transpiration-corrected convective heat transfer coefficient. It can be obtained explicitly by neglecting the radiation contribution towards the liquid film. In such a way, the transpiration correction reduces to a simpler analytical form, and the FCL can be calculated according to the following equation, without the necessity of integrating along the chamber abscissa:

$$FCL = \frac{61.62\,\mu_g}{G_{\text{mean}}}\left[\frac{\lambda^\star\,\Gamma\,Pr^{0.94}}{c_{p,g}\left(T_g - T_{sat}\right)\mu_g\left(\frac{h}{h_0}\right)}\right]^{1.25} \tag{4}$$

where μ_g is the hot gas dynamic viscosity, G_{mean} is a modified hot gas mass flux (see [9] for details), $\lambda^\star = \lambda + c_{p,liq}(T_{sat} - T_{liq})$ where λ is the latent heat of vaporization again, Γ is the liquid film mass flow rate per unit chamber circumference, $c_{p,liq}$ is the liquid film specific heat at constant pressure and T_{liq} is the liquid film injection temperature.

2.1.3 Shine model for LFC

The model by Shine et al. [10] is a 0-D analytical model for liquid film cooled combustion chambers, featuring hot-gas radiation and liquid coolant droplets entrainment into the hot gas flow. Mass transfer via entrainment is computed using the correlation by Sawant et al. [6]. Such correlation is expressed as a fraction E of the injected mass flow rate ($\Gamma_{av} = \Gamma(1-E)$, where Γ_{av} is the available mass flow rate per unit circumference). The heat exchange includes convection and radiation between the liquid film stream and the hot gas flow, assuming instantaneous heating of the liquid phase to its saturation temperature. The evaporation process is modeled similarly to Grisson model [9], i.e., calculating a dry wall convective heat transfer coefficient and then introducing a transpiration correction. The radiative

DOI: 10.13009/EUCASS2022-6165

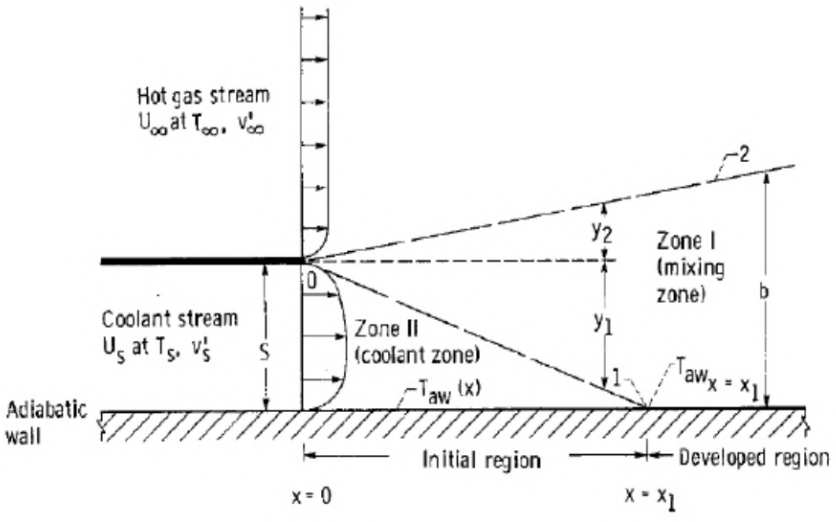

Figure 2: Geometry of the developed flow as assumed by Simon's model [17].

heat flux towards the liquid film is calculated through the Leckner correlation [44]. Once evaporation and entrainment are known, the film cooled length can be obtained as $FCL = \Gamma_{av}/\dot{m}_{vap}$. The boundary layer model is taken from the Grisson model [9].

2.1.4 Di Matteo et al. – Sapienza model for GFC

Gaseous film cooling model originally reported in Di Matteo et al. [18] has been modified in the framework of the present work. It is a quasi-2D differential-algebraic formulation for studying the shear mixing developing from a gaseous film jet, injected at the wall. The geometry of the mixing fan is based on Simon [17] (see Figure 2). He defines three different regions: core flow, film stream, and mixing region. All the three zones are assumed to share the same pressure for any given cross-section of the combustion chamber, computed neglecting the contribution of the film mass flow rate. Firstly, the length of the fresh film cooled region (x_1 in Figure 2) and the growth rate of the mixing region are calculated. The former defines the region characterized by coolant properties, so the convective heat flux is determined by the film state, while downstream the wall conditions are determined by the mixing region state. An iterative procedure [17] or a CFD-based correlation developed by Sapienza [45] can be used to evaluate x_1. The mixing zone growth rate is calculated as a function of jets densities and velocities.

The flow field geometry is shown in Figure 2. The geometry of the mixing regin, as assumed by Simon's model [17], is then computed by knowing db/dx and x_1. The least number of differential equations has been chosen to be included in the model, for simplicity and computational efficiency. In particular, mass momentum and total internal energy are retained in the core region, as in the original ESPSS combustor, whereas the film region is modelled only by means of the energy conservation law, reading

$$V_{\text{film}} \, (\rho \, \dot{e}_0)_{\text{film}} = -\Delta \, (\dot{m} \, h_0)_{\text{film}} - \dot{q}_{\text{film}} \tag{5}$$

where V_{film} is the film region volume, $(\rho \, e_0)_{\text{film}}$ is film total internal energy per unit volume, $(\dot{m} \, h_0)_{\text{film}}$ is the film total enthalpy flux, and $\dot{q}_{\text{film}}$ is the heat flux exchanged by the film region. Mass flow rate is supposed to be constant in space but variable in time, and equal to the boundary value, as if the mass flow rate information propagates with infinite speed. Knowing mass flow rate and thus mass flux $G = (\dot{m}/A)_{\text{film}}$ from the geometry, the film thermodynamic state is calculated iteratively. As in the original model [18], the mixing region properties are determined by those of the hot gas and the coolant in a one-way dependency, that means the hot gases and the coolant influence the mixing region, while the opposite dependency is neglected. Temperature in the mixing volumes is calculated as a weighted average as

$$T_i^{\text{mix}} = \frac{(T_{i-1}^{\text{mix}} \, \dot{m}_{i-1}^{\text{mix}} + T_i^{\text{film}} \, \dot{m}_i^{\text{f2m}} + T_i^{\text{core}} \, m_i^{\text{c2m}})}{(m_{i-1}^{\text{mix}} + m_i^{\text{f2m}} + m_i^{\text{c2m}})} \tag{6}$$

where superscripts f2m and c2m stand for "film-to-mix" and "core-to-mix". Since pressure is known from the core region, the density in the mixing zone can be obtained from the equation of state.

DOI: 10.13009/EUCASS2022-6165

2.2 Nozzle erosion

Three nozzle erosion models have been selected and implemented in the ESPSS framework, according with their architecture. The implementation has been carried out within the original solid/hybrid thrust chamber super-components [46], without altering in any significant way their original structure. Hence, all the original flow models have been retained, and the ablative subroutines can be simply activated or deactivated. They act modifying the combustor geometry at each time step The models have limitation, in fact some of them can be used only for SRM applications, while others only for HRE ones. In the following, the different models implemented are described in details.

2.2.1 Semi-empirical correlations

Semi-empirical correlations are zero-dimensional models for nozzle throat erosion rate calculation. Two different ones have been identified in the literature and implemented, one for SRMs [36, 37] and one for HREs [38]. Concerning SRMs, the selected correlation calculates nozzle throat erosion rate $\dot{r}_{th}$ as a function of chamber pressure p_c, nozzle geometrical characteristics, and concentration of water vapor in the free-stream [36, 37]:

$$\dot{r}_{th} = 1.4732 \cdot 10^{-5} \, M_{H_2O} \left(\frac{p_c}{p_{c,ref}} \right)^{0.8} \left(\frac{D_{th,ref}}{D_{th}} \right)^{0.2} \left(\frac{D_{th,ref}}{D_{th}} \frac{R_c}{R_{c,ref}} \right)^{0.1} \left(\frac{\rho_{c,ref}}{\rho_c} \right) (1+\varphi)^{-1} \tag{7}$$

where M_{H_2O} is the mole percentage of water vapor in the gaseous mixture at throat, D_{th} is the nozzle throat diameter, R_c is the nozzle curvature radius, ρ_c is the ablative material char density, and φ is the pyrolysis to char mass flow rate ratio [30]. The subscript *ref* indicates reference quantities.

On the other hand, concerning HREs, the selected semi-empirical correlation calculates nozzle throat erosion rate as a function of the chamber pressure, of the nozzle geometrical characteristics, and of the equivalence ratio [38]:

$$\dot{r}_{th} = \frac{K_1}{\rho_c \, (1+\varphi)} \left[\left(\frac{3.42}{\phi} \right)^{-1.125} \; 10^{\left(\frac{-3.157\,\phi}{3.42} - 0.1557 \right)} \quad p_c^{\,K_2 \left(0.00174 \left(\frac{3.42}{\phi} \right)^2 - 0.05301 \left(\frac{3.42}{\phi} \right) + 1.119 \right)} \right] \tag{8}$$

where K_i are user defined coefficients to take into account nozzle geometrical effects, and ϕ is the equivalence ratio. The inclusion of the equivalence ratio dependence is of fundamental importance as throttling and mixture ratio shift are intrinsic characteristics of HRE [29].

Moreover, both the correlations have some constrains on propellant. In particular, Eq. (7) can be used only in case of grains employing metal powders (i.e., aluminum) and ammonium perchlorate as oxidizer [36]. On the other hand, Eq. (8) is valid only for HRE in which oxygen is employed as oxidizer [38].

Even if those correlations are defined only for the throat section, a simple correction based on the Bartz law [47] can be used to extend them to the generic *i*-th nozzle axial section.

$$\dot{r}_i = \dot{r}_{th} \, (A_i / A_{th})^{-0.9} \tag{9}$$

2.2.2 B' tables model

The B' tables model [19] relies on the coupled solution of the Surface Mass Balance (SMB) and Surface Energy Balance (SEB), which employ transfer coefficients to capture the effects of the species diffusion through the chemical boundary layer, and the heat transfer through the thermal boundary layer. In the B' model, the solution of the SMB is tabulated in the so called B' thermochemical equilibrium tables. The B' parameter (or dimensionless ablation mass flux B') listed in the tables is calculated (for a non-pyrolyzing carbon-based material) as:

$$B' = \frac{\dot{m}_w}{\rho_e \, u_e \, C_m} = \frac{Y_{kw} - Y_{ke}}{Y_{kc} - Y_{kw}} = \frac{Y_{kw} - Y_{ke}}{1 - Y_{kw}} \tag{10}$$

where $\dot{m}_w$ is the overall ablation mass flux, C_m is the dimensionless mass transfer coefficient, and Y_k is the elemental mass fraction of the *k*-th chemical element. The subscripts *w*, *e*, and *c* stand for wall, boundary layer edge, and solid material at the wall, respectively. Hence, the mass fractions of the *k* chemical elements considered in the problem are needed to compute the B' tables. Such computation can be done offline using a chemical equilibrium code (e.g.,

DOI: 10.13009/EUCASS2022-6165

CEA [48]), for different pressures and temperatures. It is worth noting how different tables are needed for different propellant formulations. For this reason, only a limited number of tables have been included within the ESPSS libraries, covering the most diffused SRM propellant formulations.

The SEB, solved accordingly to the tabulated SMB solutions listed in the B' tables, reads as

$$\rho_e\, u_e\, C_h\, (h_r - h_{ew}) + \rho_e\, u_e\, C_m \left(h_{ew} - h_w + B'\, h_{sw} - B'\, h_w\right) = \sigma\, \varepsilon\, T_w^4 + \dot{q}_{\mathrm{cond,w}} \tag{11}$$

where C_h is the dimensionless heat transfer coefficient, h_r is the recovery enthalpy, and $\dot{q}_{\mathrm{cond,w}}$ is the heat conduction term. C_h is obtained by means of the Bartz correlation.

In order to take into account non-negligible boundary-layer development effects two correction factors have been included in the Bartz correlation, taking into account wall entrance length and contraction ratio effects [49]. They read

$$K_a = \left(\frac{R_{in}}{L_{en}}\right)^{0.2} \quad ; \qquad K_b = \left(\frac{R_{th}}{R_{in}}\right)^{0.05} \tag{12}$$

$$\rho_e\, u_e\, C_{h_0} = \frac{h_{c,m}}{c_p} = \frac{h_c\, K_a\, K_b}{c_p} \tag{13}$$

where h_c is the regular Bartz coefficient [47], R_{in} is the nozzle radius at nozzle inlet, and L_{en} is the wall entrance length from nozzle inlet up to throat.

A blowing correction is also included [19] to consider the blockage effect due to the surface ablation:

$$\frac{C_h}{C_{h_0}} = \frac{\zeta}{\mathrm{e}^{\zeta} - 1} \quad ; \qquad \zeta = \frac{2\, \lambda\, \dot{m}_w}{\rho_e\, u_e\, C_{h_0}} \tag{14}$$

where λ is a semi-empirical parameter, typically assumed equal to 0.4 in case of turbulent flow [19]. The dimensionless mass transfer coefficient C_m is then evaluated from of C_h by means of the Chilton-Colburn relation [19] assuming a constant Schmidt number of 0.7.

The wall temperature T_w represents the unknown of the iterative problem, to satisfy the SEB. The B' parameter is obtained by run-time interpolating the B' tables using the local pressure and a tentative wall temperature. Once the correct wall temperature value is obtained, the recession rate can be evaluated from the correspondent B' parameter:

$$\dot{r} = \frac{B'\, \rho_e\, u_e\, C_m}{\rho_c\, (1 + \varphi)} \tag{15}$$

2.2.3 Simplified kinetic chemistry model

The simplified kinetic chemistry model (FRchem) originally proposed in [42] has been enriched in the frame of this activity, in order to improve its applicability range and its overall predictive capability, including a chemical boundary layer model. Neglecting it is a good assumption only if ablation is strongly kinetic-limited, where the chemical composition inside the boundary layer is expected to be almost coincident with external one (species are consumed slowly at the wall, while diffusion is faster). On the other hand, chemical composition gradients in the boundary layer are higher if ablation is diffusion-limited, yielding the original model [42] to overpredict the material ablative response. The final result is a model with basically no limitations, similar to those employed in state-of-art ablative CFD codes [25, 29], relying on few semi-empirical factors modeling mass and heat transport phenomena.

In the final model, the thermo-chemical ablation is computed solving both SMB and SEB, reading

$$\rho_e\, u_e\, C_m\, (Y_{ie} - Y_{iw}) + \dot{\omega}_i = \dot{m}_w\, Y_{iw} \tag{16}$$

$$\rho_e\, u_e\, C_h\, (h_r - h_{ew}) + \rho_e\, u_e\, C_m\, (h_{ew} - h_w) + \dot{m}_w\, h_{sw} = \dot{m}_w \left(h_{sw} - h_{s_0}\right) + \dot{m}_w\, h_w + \sigma\, \varepsilon\, T_w^4 \tag{17}$$

where Y_i is the mass fraction of the i-th species. The dimensionless parameters C_h and C_m read as in the B' tables model (see Eqs. (12), (13) and (14)). Differently from the B' tables approach, surface conditions, including the surface heat fluxes and ablation rate, are determined based on a finite-rate surface reaction mechanism. A semi-global graphite oxidation kinetics for non-porous graphite is used [50] (see Table 1). With this mechanism, the contribution to carbon erosion due to the i-th species [29] can be expressed as:

DOI: 10.13009/EUCASS2022-6165

Table 1: Heterogeneous rate constants of carbon with the main oxidizing species.

Surface reaction	j	A_j	E_j, kJ/mol	b_j	n_j
$C_s + H_2O \rightarrow CO + H_2$	1	4.8 e5	288	0.0	0.5
$C_s + CO_2 \rightarrow 2CO$	2	9.0 e3	285	0.0	0.5
$C_s + OH \rightarrow CO + H$	3	3.61 e2	0.0	-0.5	1.0
$C_s + O \rightarrow CO$	4	6.655 e2	0.0	-0.5	1.0
$C_s + 0.5\,O_2 \rightarrow CO$	5	2.4 e3	125.6	0.0	0.5
	6	2.13 e1	-17.17	0.0	0.5
	7	5.35 e-1	63.64	0.0	0.5
	8	1.81 e7	406.1	0.0	0.5

$$\dot{m}_{i,w} = k_j \, p_i^{n_j} \qquad \text{for } i = \{H_2O, CO_2, OH, O\} \tag{18}$$

$$\dot{m}_{i,w} = \frac{k_5 \, p_i \, Z}{1 + k_6 \, p_i} + k_7 \, p_i \, (1 - Z) \quad ; \qquad Z = \left(1 + \frac{k_8}{k_7 \, p_i}\right)^{-1} \qquad \text{for } i = O_2 \tag{19}$$

where p_i is the partial pressure (in atm) of the oxidizing species i, and k_j is the rate constant of the j-th reaction expressed by an Arrhenius. The overall ablation mass flux of carbon due to the surface heterogeneous reactions can be expressed as a sum of the terms in Eqs. (18) and (19).

The final result from the coupling between the SMB and the finite-rate chemistry model is something similar to the B' thermochemical tables, which are "generated on-the-fly" at each time-step without the assumption of chemical equilibrium, and for any propellant combination, without limitations. The main drawback is the needed computational effort, since the SMB, the SEB and the finite-rate chemistry are coupled in a non-linear fashion, hence they must be solved jointly in an iterative way.

Once the overall ablation mass flux $\dot{m}_w$ is obtained, the erosion rate is calculated as

$$\dot{r} = \frac{\dot{m}_w}{\rho_c \, (1 + \varphi)} \tag{20}$$

3. Validation test cases

In the present section the selected test cases, used for the models validation procedure are presented, for both chamber film cooling and nozzle erosion.

3.1 Film cooling

Experimental test cases have been selected from the literature to validate the models presented above for liquid and gaseous film cooling. An overview of the chosen test cases is provided in the following. The selected test cases include two tests for liquid film cooling [51, 52] and two tests for gaseous film cooling [53, 54]:

3.1.1 Morrell

The investigation [51] consists in a series of four tests employing a liquid oxygen/liquid ammonia thrust chamber, using water as coolant. Wall heat load, thrust, and film cooled length are evaluated in an 8.5 inches long test section located downstream of the injection plate. Coolant injection occurs by means of tangential-slot injectors at the beginning of the test section. Investigations have been performed using different propellant and coolant mass flow rates (see Table 2 – more details in [51]). Available observables are the film cooled length, the thrust, and the integral heat load. The heat load measure is deduced from temperature measurements performed with thermocouples, and adding the vaporization heat where the liquid phase is present. No details on the temperature and heat profiles are reported.

3.1.2 Kim et al.

Test hardware features a film and regeneratively cooled-liquid oxygen/kerosene calorimetric combustion chamber [52]. Operating conditions are shown in Table 3. Operating conditions used in [52]. Kerosene is used as film coolant and it is injected tangentially at the injector plate, whereas ambient-temperature water is used in the 19 cooling channels

DOI: 10.13009/EUCASS2022-6165

Table 2: Operating conditions used in [51].

Test no.	Oxidizer mfr (kg/s)	Fuel mfr (kg/s)	Film mfr (kg/s)
# 8	0.99	0.70	0.836
# 9	1.05	0.69	0.836
# 10	1.16	0.66	0.093
# 11	1.14	0.68	0.095

circuits. Cooling channels are used during the experiment to provide heat flux measurements, which are performed by evaluating the total enthalpy difference between the cooling circuits manifolds. The presence of many cooling circuits ensures a good spatial resolution for measurements. Observables are the average hot gas side wall temperature, characteristic velocity, and the axial profiles of wall heat flux.

Table 3: Operating conditions used in [52].

Chamber pressure (bar)	O/F	Oxidizer mfr (kg/s)	Fuel mfr (kg/s)	Film mfr (kg/s)
52.5	2.77	4.42	1.59	0.166

3.1.3 Arnold et al.

The experiment is an investigation of film cooling performances in a high-pressure liquid oxygen/gaseous hydrogen combustion chamber made up by 5 segments [53]. Coolant is gaseous hydrogen, which is injected at the injection plate by means of 10 rectangular slots. Information about heat load distribution is provided on the hot inner surface of the combustion chamber. Chamber pressure is 115 bar. Operating conditions are shown in Table 4. Available observables are axial measurements of wall heat flux. Hot gas-side wall temperature is provided so it is possible to use it as boundary condition to retrieve the heat flux numerically.

Table 4: Operating conditions used in [53].

Oxidizer mfr (kg/s)	Fuel mfr (kg/s)	Film mfr (kg/s)
3.6	0.6	0.084 (2% tot)

3.1.4 Suslov et al.

Film cooling performances in a low-pressure gaseous oxygen/gaseous methane combustor are investigated in [54]. Operating conditions are shown in Table 5. Coolant is ambient-temperature methane, which is injected at the injection plate by means of a ring injection slot. The investigation focuses on the interaction of the reacting flow with film cooling in the cylindrical part of the combustion chamber near the injector plate, eventually providing information on heat loads distribution at chamber pressures up to 12 bar. Hot gas-side wall temperature is provided so it is possible to use it as boundary condition to numerically retrieve the heat flux, provided as well.

Table 5: Operating conditions used in [54].

Oxidizer mfr (kg/s)	Fuel mfr (kg/s)	Film mfr (kg/s)	Film injection slot height (mm)
0.335	0.1	0.087 (20% tot)	0.46

DOI: 10.13009/EUCASS2022-6165

3.2 Nozzle erosion

Concerning nozzle erosion, the following three SRM test cases and two HRE test cases have been selected from the literature, for the validation procedure of the reduced nozzle erosion models implemented in the ESPSS libraries.

3.2.1 ISPM solid rocket motor

A series of tests have been done on the ISPM motor [31,55] employing a solid propellant without metal additives (13% HTPB, 87% Ammonium perchlorate (AP)), including different chamber pressure levels. A graphitic nozzle with a bulk density of 1920 kg/m^3 is used in all tests. Experimental averages of throat erosion rates are available for validation. Two test cases, characterized by substantially different conditions in terms of chamber pressure, have been considered (see Table 6).

Table 6: Operating conditions used in [31, 55].

	Test. ISPM-01	Test. ISPM-07
D_{th}, cm	1.27	1.27
R_{in}, cm	1.0	1.0
L_{en}, cm	14.8	14.8
p_c, bar	64.4	162.8
$\dot{r}_{th}$, mm/s	0.162	0.261 (±22.6%)
η_{c*}, - [13]	0.937	0.940

3.2.2 BATES solid rocket motor

A series of tests employing different solid propellant formulations including metal additives (HPTB, AP, and aluminum powder) have been performed on the BATES motor [36, 56]. A graphitic nozzle with a bulk density of 1830 kg/m^3 is used in all tests. Experimental averages of the throat erosion rate are available for validation. Three tests have been considered, whose main data are summarized in Table 7.

Table 7: Operating conditions used in [36, 56].

	HTPB 1510	HTPB 1810	HTPB 2110
D_{th}, cm	5.08	5.08	5.08
% Al	15	18	21
p_c, bar	69	69	69
$\dot{r}_{th}$, mm/s	0.35	0.28	0.20
Y_{H_2O}, -	0.145	0.105	0.07
η_{c*}, - [32]	0.98	0.95	0.94

3.2.3 Hippo solid rocket motor

A firing test of the Hippo motor [57] has been performed, employing a metallized solid propellant (12% Poly-Butadiene Acrylo-Nitrile copolymer (PBAN), 2% of epoxy curing agent, 70% AP, and 16% aluminum powder). A carbon-phenolic nozzle is employed, with a virgin density of 1462 kg/m3 and a char density of 1173 kg/m3 (i.e., φ = 0.246). The experimental chamber pressure trace is provided in [57] and the experimentally measured erosion all along the nozzle length is available for validation [57]. Hence, this test case can be used in order to assess the nozzle shape change capabilities, included in the ESPSS libraries.

3.2.4 Hokkaido University HDPE/LOX hybrid rocket engine

A series of 2kN thrust-class HDPE/LOX HRE firing tests have been done at the Hokkaido University [38] using different nozzle geometries and covering a wide range of average mixture ratio and chamber pressures conditions. A graphitic nozzle is used, with a bulk density of 1850 kg/m3. Experimental averages of nozzle throat erosion rate are

DOI: 10.13009/EUCASS2022-6165

available for validation. In particular, three test cases, characterized by substantially different conditions in terms of oxidizer-to-fuel mixture ratio (see Table 8).

Table 8: Operating conditions used in [38].

	Test A-2	Test A-5	Test B-7
D_{th}, cm	2.70	2.70	1.98
R_{in}, cm	3.30	3.30	6.50
L_{en}, cm	4.01	4.01	12.03
p_c, bar	19.79	16.07	29.85
O/F, -	3.71	5.86	1.07
$\dot{r}_{th}$, mm/s	0.215 (±24.4%)	0.134 (±36.8%)	0.0 ± 0.02

3.2.5 Hokkaido University HDPE/N2O hybrid rocket engine

A series of 100N thrust-class HDPE/N2O HRE firing tests covering a wide range of average mixture ratio and chamber pressures conditions have been performed at the Hokkaido University [39]. A graphitic nozzle is used, with a bulk density of 1850 kg/m3. Experimental averages of nozzle throat erosion rate and throat wall temperature are available for validation. In particular, three test cases have been considered, briefly summarized in Table 9.

Table 9: Operating conditions used in [39].

	Test C-1	Test C-2	Test C-3
D_{th}, cm	0.4	0.4	0.4
R_{in}, cm	1.4	1.4	1.4
L_{en}, cm	6.4	6.4	6.4
p_c, bar	32.17	27.67	43.81
O/F, -	8.35	9.02	7.14
$\dot{r}_{th}$, mm/s	0.143 (±10.0%)	0.135 (±6.1%)	0.165 (±21.8%)

4. Results of the validation procedure

In the present section the discussion of the results of the validation procedure is reported, for both film cooling and nozzle erosion.

4.1 Liquid Film Cooling validation

Starting with LFC, experimental data by Morrell [51] are compared to numerical results in Table 10. The mixing process between the coolant and the hot gas provides a good estimation of the thrust which is in good agreement with experimental data for all the three LFC models for each test. In fact, all the three formulations model the chamber pressurization due to coolant injection. Film cooled length tends to be overestimated by all the models, in each test case, even if acceptable ranges of errors are provided (average is of about 15%). As expected, the best evaluations are provided by the most detailed model, i.e., Grisson model in full formulation. As expected, 0-D models (Simplified Grisson and Shine et al) return higher errors with respect to Grisson full formulation due to their higher level of simplification. They show a significantly similar behavior dealing with this specific test case. Between the two, Shine model seems to give a slightly better accuracy in the FCL estimation.

Full Grisson model is the only one that can be considered reliable when comparing integral heat loads, since it employs a specific and detailed modeling for the estimation of the heat exchange coefficients. Moreover, it gives the best estimation of the FCL, which is a key parameter when comparing the integral heat load since the temperatures of the liquid phase and of the evaporated boundary layer might be significantly different, strongly influencing such an observable.

DOI: 10.13009/EUCASS2022-6165

Table 10: Experimental and estimated observables by Morrell [51] and present LFC models. "Q" stands for integral heat load.

	TEST #8				TEST #9			
	EXP	Full Grisson	Simplified Grisson	Shine et al	EXP	Full Grisson	Simplified Grisson	Shine et al
Thrust, kgf	404.6	382.3	381.4	391.7	397.3	384	383.4	383.6
Error, %	-	-5.52	-5.73	-5.65	-	-3.34	-3.49	-3.45
FCL, m	0.1879	0.2167	0.221	0.2193	0.2073	0.2236	0.2343	0.229
Error, %	-	15.32	17.61	16.71	-	7.86	13.03	10.46
Q_tot, BTU/lb	876	829.9	not reliable	not reliable	871	823.2	not reliable	not reliable
Error, %	-	-5.26	-	-	-	-5.49	-	-
Q_conv, BTU/lb	732	706.9	not reliable	not reliable	736	701.74	not reliable	not reliable
Error, %	-	-3.42	-	-	-	-4.65	-	-
Q_rad, BTU/lb	144	123	not reliable	not reliable	135	121.47	not reliable	not reliable
Error, %	-	-14.55	-	-	-	-10	-	-
	TEST #10				TEST #11			
	EXP	Full Grisson	Simplified Grisson	Shine et al	EXP	Full Grisson	Simplified Grisson	Shine et al
Thrust, kgf	415.9	393.88	393.53	394	415.9	397.56	397	397
Error, %	-	-5.29	-5.37	-5.27	-	-4.40	-4.54	-4.54
FCL, m	0.2042	0.2419	0.2671	0.2549	0.2174	0.2411	0.2663	0.2537
Error, %	-	18.46	30.8	24.82	-	10.90	22.49	16.69
Q_tot, BTU/lb	856	559	not reliable	not reliable	856	560	not reliable	not reliable
Error, %	-	-34.69	-	-	-	-34.58	-	-
Q_conv, BTU/lb	731	450	not reliable	not reliable	721	456.02	not reliable	not reliable
Error, %	-	-38.44	-	-	-	-36.75	-	-
Q_rad, BTU/lb	125	110	not reliable	not reliable	135	103.9	not reliable	not reliable
Error, %	-	-12	-	-	-	-23.04	-	-

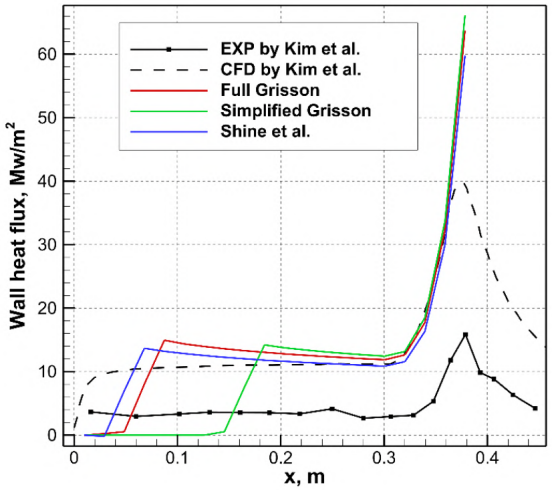

Figure 3: Comparison between experimental [52] and numerical results. CFD by Kim et al. is also included

DOI: 10.13009/EUCASS2022-6165

Table 11: Comparison between Kim et al. [52] scalar observables and numerical results.

	EXP	Full Grisson	Simplified Grisson	Shine et al.
Average Tw [K]	610	668,2	576,8	796
Error (%)	-	9,54	-5,44	30,49
Characteristic velocity (m/s)	1670	1730	1728	1702
Error (%)	-	3,59	3,47	1,91

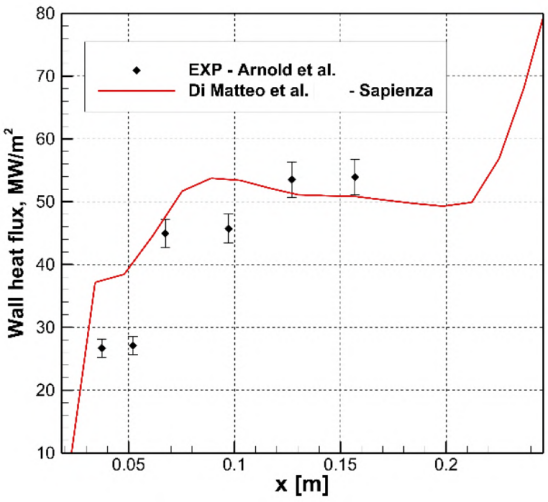

Figure 4: Comparison between experimental data by Arnold et al. [53] and numerical results.

Comparisons between Kim et al. scalar observables [52] and numerical results are listed in Table 11 and shown in Figure 3. Performances, in terms of characteristic velocity, are well predicted by each of the three models. Errors are confined below the 4% threshold. This proves that the assumptions made on the mixing process between the evaporated coolant and the hot gases are appropriate.

Also wall temperatures are in good agreement with experimental data. As expected, also here the complete Grisson model shows the best results with an error of 9.5% with respect to the experiment, whereas the highest discrepancy is showed by Shine model which overestimates the wall temperature by a factor of 30.5%.

The lowest error on the average wall temperature prediction is provided by the Simplified Grisson model, which provides a better prediction than the full formulation. Although the temperature averaging process is not explained in detail in the paper, this aspect is quite unexpected because of the low reliability expected by 0-D models concerning heat transfer evaluation. One possible explanation might lie in the interplay of two different errors. On one hand, 0-D models (as Shine et al.) generally tend to overestimate wall temperature. On the other hand, simplified Grisson model provides a higher film cooled length (FCL) than the other two models, as can be observed from the plot in Figure 3, thus considering a higher wall region with lower temperature, which contributes to decrease the average value in the combustion chamber. As a possible consequence of this combined and counterbalanced effect, what is observed is an average wall temperature which is close to experimental data. The effect might be case dependent.

Concerning convective heat fluxes, all the three liquid film cooling models (red, green, and blue solid lines in Figure 3) provide similar results and overestimate experimental data (black solid line with symbols). However, it must be pointed out that the results are in good agreement with the simulations performed by Kim et al. and reported in the paper. Such fact might be due to some physics happening in the experiment which is not properly modeled numerically.

4.2 Gaseous Film Cooling validation

Concerning to GFC, comparisons between experimental data by Arnold et al. [53] and numerical results obtained by means of the Di Matteo et al. [18] – Sapienza model are shown in Figure 4. Numerical solution is in overall good agreement with experimental data, which are also affected by some uncertainty. The maximum punctual error is in the

DOI: 10.13009/EUCASS2022-6165

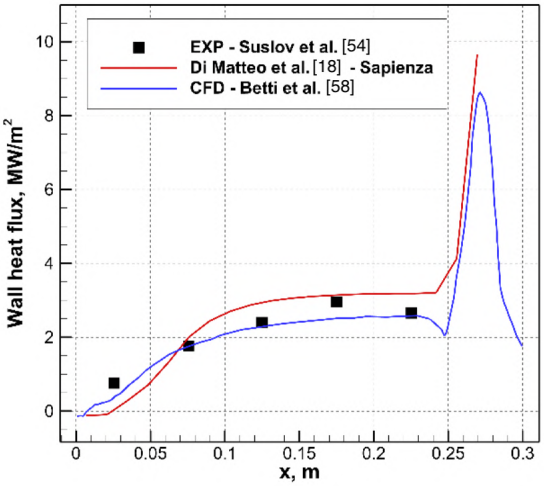

Figure 5: Comparison between experimental data by Suslov et al. [54], reduced model numerical results, and CFD simulation by Betti et al. [58].

range of 17% and it is obtained in the fully mixed region. Heat flux trend is well predicted. The model is capable of capturing the heat flux ramp in the vicinity of the injection plate due to combustion development and also to the film presence, in this case.

Even if no measurement point is available in the nozzle, the higher the heat flux values are, the lower the error seems to be. In particular, the last two measurement points values are reproduced within their experimental error bars.

Lastly, the comparison between experimental data by Suslov et al. [54] and numerical results, for the oxygen/methane propellant combination, are shown in Figure 5. A CFD simulation performed by Betti et al. [58] regarding the same test case and operating conditions is also shown.

Experimental wall heat flux is well reproduced by the gaseous film cooling model by Di Matteo et al. [18] and Sapienza. The maximum punctual error is in the range of 19% with respect to the experimental data, and it is obtained downstream in the fully mixed region. The typical initial heat release ramp due to combustion development and to the film presence and mixing is well captured. A higher film extension is obtained by the numerical model (red line), and thus higher errors are shown close to the injection region. Errors with respect to experiments appear to be of the same order of magnitude of the ones obtained with the more complex CFD simulation, confirming the reliability of the approach.

A second configuration is used to assess the validity of the GFC reduced model in case of oxygen/methane. Such configuration foresees the same propellant mass flow rates shown in Table 5. Operating conditions used in [54], but using a lower film mass flow rate of 0.022 kg/s (i.e. 5% of the total mass flow rate) and a film injection slot height of 0.2 mm. CFD simulations have been performed to provide a term of comparison for the GFC reduced model results. Comparison between the results and the CFD simulations are shown in Figure 6.

Reduced model solution (red line) is in good agreement with that provided by CFD simulation (black line). The maximum punctual error is in the range of 18% with respect to the simulation results. A further solution without film cooling (blue line) is included in the comparison to show the influence of coolant injection on the wall heat flux. Although some discrepancies are present, wall heat flux trend is well predicted. Particular precision is shown approaching the plateau in the first half of the chamber, where the two solutions (red and black lines) are almost overlapped.

By looking at both Figure 5 and 6, it can be said that the Di Matteo-Sapienza model is validated against gaseous film cooling test cases, showing an accuracy with respect to experimental data which is comparable to that of more complicated CFD simulations.

4.3 Nozzle erosion of solid rocket motors validation

The first test case analyzed for the nozzle erosion models validation in SRM environment is the ISPM motor test campaign [55]. Only two nozzle erosion models have been used for the ISPM motor simulations: the B' tables model and the FRchem model. The semi-empirical correlation for SRM has not been considered as it can be used only in

DOI: 10.13009/EUCASS2022-6165

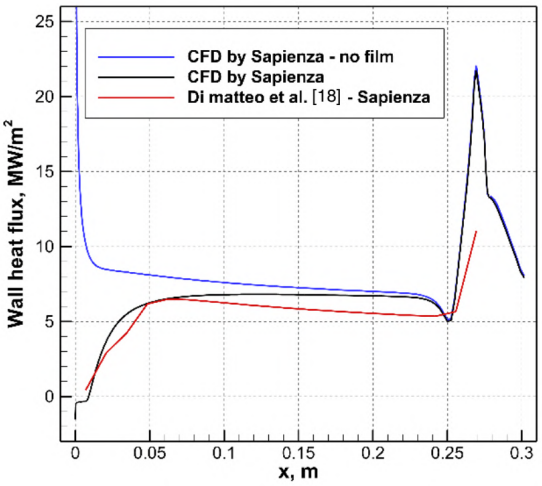

Figure 6: Comparison between reduced model results and CFD simulations.

Table 12: Nozzle throat erosion rates obtained from the ESPSS simulations for the two ISPM motor tests considered (see Table 6) and comparison with experimental data.

$\dot{r}_{th}$, mm/s	Test ISMP-01	Test ISPM-07
exp. [30]	0.162	0.261 (±22.6%)
B' model (η_{c*}=1)	>0.64	>1.18
B' model (η_{c*}≠1)	-	-
FRchem (η_{c*}=1)	0.177 (+9.3%)	0.406 (+55.5%)
FRchem (η_{c*}≠1)	0.148 (-8.6%)	0.330 (+26.4%)

case of metallized solid propellants. The main results obtained for the two test cases in Table 6 are summarized in Table 12. Considering the B' tables model, extremely high throat erosion rates have been reported (even three times higher than the FRchem model ones). In fact, it is known how the equilibrium B' tables model leads to reliable results only in the diffusion-limited ablation regime, which is usually the case of SRM using metallized solid propellants [25]. Concerning the ISPM motor tests under investigation, a non-metallized solid propellant is used, and the ablation process is kinetic-limited.

Hence, as expected, results obtained using the B' model are not representative of the actual physical phenomenon. Looking to the FRchem model results in Table 12, concerning the ISPM-01 test case, numerical and experimental data are in good agreement for both unitary and non-unitary combustion efficiencies (+9.3% and -8.6% respectively). On the other hand, concerning the ISPM-07 test case, throat erosion rate is largely overestimated when an unitary combustion efficiency is considered (+55.5%, which is outside of the ±22.6% experimental uncertainty bar). However, by including the effects of a non-unitary combustion efficiency, an acceptable agreement with the experimental data is obtained, with a +26.4% overestimation, close to the experimental uncertainty.

In conclusion, the FRchem model can be assumed to be validated concerning SRM applications employing non-metallized solid propellants. Moreover, it has been clarified how the FRchem model is the only valuable choice for nozzle erosion simulations in case of non-metallized solid propellants. The ISPM motor has been used in order to assess the ESPSS predictive capabilities in terms of boundary-layer development effects on the throat erosion rate. These effects are accounted for thanks to the correction factors introduced in the Bartz correlation (see Eq. (12)). To this purpose, ESPSS results have been compared with CFD computations available in literature [31]. In Figure 7, wall entrance length has been made dimensionless using the actual wall entrance length L_{en} of the ISPM motor.

The agreement between ESPSS and CFD results is significantly good, hence wall entrance length effects are correctly captured by the low-order model, using the correction factors in Eq. (12). It is worth noting how if the Bartz correlation not employing the correction factors is used, the throat erosion rate of the full wall entrance length ISPM motor is overestimated of approximately 70%. Hence, this underlines how boundary-layer development effects are of fundamental importance in ablative calculations and must be taken into account.

The second test campaign analyzed for the nozzle erosion models validation in SRM environment is the BATES motor [36], which employs metallized solid propellants. Three nozzle erosion models have been used for the BATES

DOI: 10.13009/EUCASS2022-6165

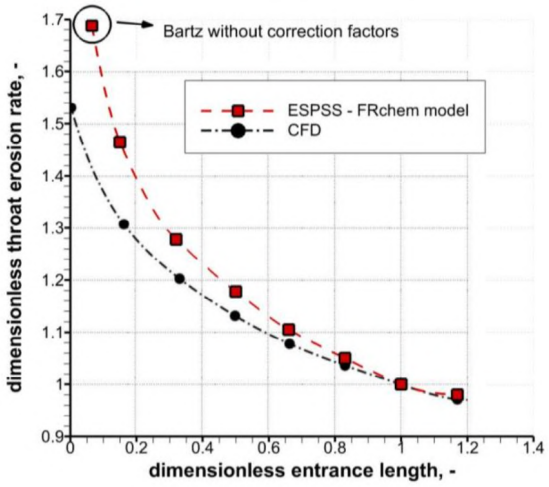

Figure 7: Wall entrance length effects on throat erosion rate according to the ESPSS and CFD simulations [31] for the ISPM motor.

Table 13: Nozzle throat erosion rates obtained from the ESPSS simulations for the three BATES motor tests considered (see Table 7) and comparison with experimental and CFD data.

$\dot{r}_{th}$, mm/s	HTPB 1510	HTPB 1810	HTPB 2110
exp. [18]	0.35	0.28	0.20
CFD eql [8]	0.396 (+12.2%)	0.291 (+2.1%)	0.194 (-3.0%)
CFD f.r. [8]	0.349 (-1.1%)	0.274 (-3.9%)	0.193 (-3.5%)
Semi-empirical	0.373 (+5.7%)	0.295 (+3.5%)	0.210 (+5.0%)
B' model (eql.)	0.48 (+35.9%)	0.376 (+31.9%)	0.253 (+26.5%)
FRchem (f.r.)	0.33 (-6.5%)	0.301 (+5.6%)	0.261 (+30.5%)

motor simulations: the semi-empirical correlation for SRM (see Eq. (7)), the B' tables model, and the (FRchem) model.

The main results obtained for the three test cases in Table 7 are summarized in Table 13. For all the test cases analyzed, the ESPSS model performing better with respect to the experimental data is the semi-empirical one, with a maximum discrepancy in terms of throat erosion rate of +5.7%. An interesting aspect has to be underlined by looking to the B' and FRchem model results. The erosion rates at throat computed with the chemical equilibrium approach (i.e., B' model) show a monotonically decreasing discrepancy with respect to the experimental data as the aluminum content is increased. This trend has been noticed as well in CFD computations [26]. The reason is the importance of the surface chemical kinetics in case of low aluminum contents (i.e., 15% Al, HTPB 1510), as in this case wall temperature is lower and ablation is kinetic-limited. Moving towards 18% and 21% Al, the ablation process passes gradually from being kinetic-limited to become diffusion-limited. In fact, wall temperature increases due to the higher flame temperature (ensured by the major aluminum content) and to the lower erosion rate (ensured by the lower content of oxidizing species). In case of a diffusion-limited ablation regime, results from the surface equilibrium model are expected to be more reliable. This has been observed in the CFD simulations [26] and has been confirmed as well by the ESPSS results. In fact, the erosion prediction with the finite-rate model (i.e., FRchem) is almost exactly superimposed to its surface equilibrium counterpart (i.e., B' model) in case of the higher aluminum content (i.e., 21% Al, HTPB 2110). It is worth noting how all models are capable to correctly capture the variation of the throat erosion rate at varying solid propellant formulation. Therefore, even if errors in terms of throat erosion are obtained in some cases (with a maximum discrepancies of +35.9%), it can be concluded how results of the ESPSS simulations compare well with the experimental data.

The last experimental test analyzed for the nozzle erosion models validation in SRM environments is the Hippo motor [57]. This test case has been used in order to verify the reliability of the full-nozzle shape change capabilities

DOI: 10.13009/EUCASS2022-6165

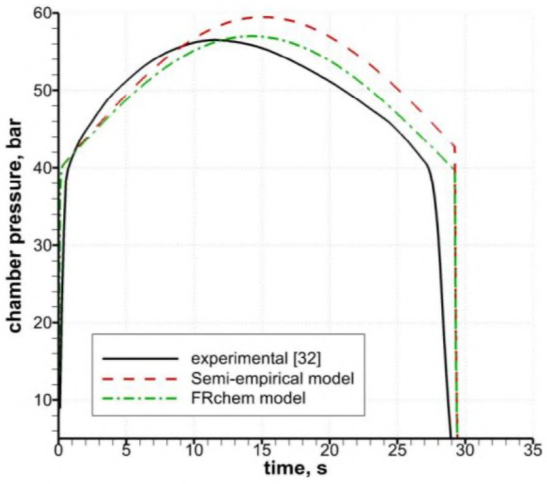

Figure 8: Comparison between the experimental chamber pressure trace and the chamber pressure time histories obtained using different ESPSS nozzle erosion models.

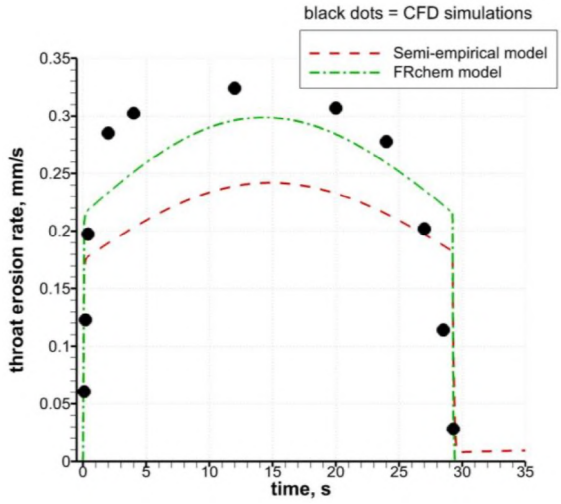

Figure 9: Comparison between nozzle throat erosion rates obtained from CFD simulations and ESPSS computations for the Hippo motor.

included in the ESPSS. Two nozzle erosion models have been used for the Hippo motor simulations: the semi-empirical correlation for SRM and the FRchem model.

A first effort has been dedicated in rebuilding the experimental chamber pressure time history. In fact, as the nozzle shape change has to be predicted, a time-accurate rebuilding of the whole motor firing is required. Hence, the nozzle grain geometrical characteristics have been rebuilt in order to match as much as possible the experimental chamber pressure (including nozzle throat erosion effects). The reference ablative model considered in the grain geometry rebuilding is the FRchem model. The chamber pressure time history obtained is reported in Figure 8. It is worth noting how a slight chamber pressure overestimation can be observed for the semi- empirical correlation model, as in this case the calculated nozzle throat erosion is lower (see Figure 8). Anyway, looking at the throat erosion rate time histories reported in Figure 8, it can be appreciated how the calculations performed in the ESPSS are in good agreement with the CFD simulations performed using an in-house RANS-based CFD solver.

Figure 10 shows the erosion rate distributions along the nozzle length at different times according to CFD and ESPSS calculations. Here, it can be observed how the variations of the erosion rate distribution over time are well captured in the ESPSS, as both semi-empirical and FRchem models show an erosive behavior in time qualitatively similar to the CFD, with a maximum erosion rate at around 12 seconds.

In Figure 11, erosion rate distributions at the initial (0.2 seconds) and final (28 seconds) times have been made dimensionless using the correspondents throat erosion rates as reference values. By doing this, the effect of the nozzle

DOI: 10.13009/EUCASS2022-6165

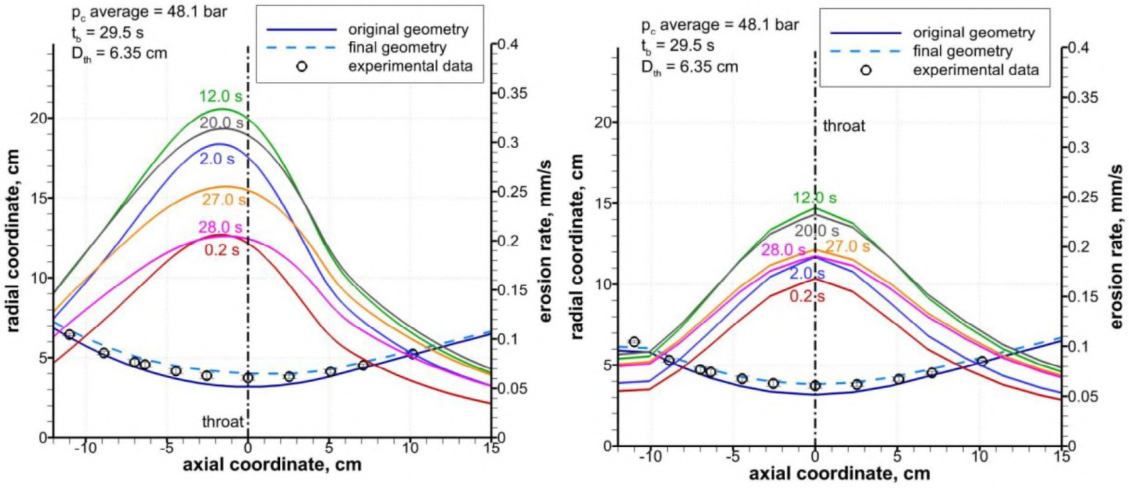

(a) CFD.

(b) ESPSS – semi-empirical.

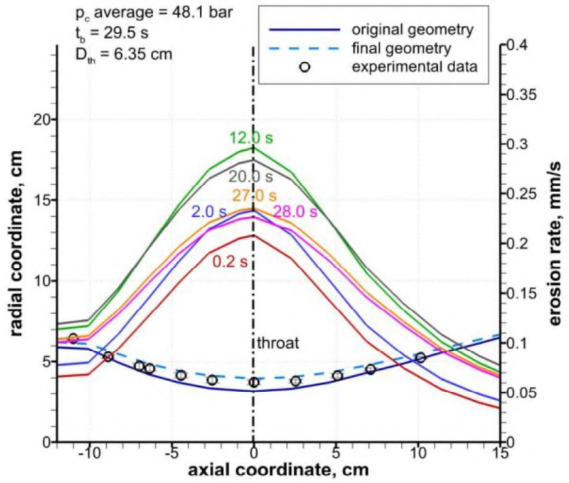

(c) ESPSS–FRchem model.

Figure 10: Erosion rate distributions along the nozzle length at different times according to CFD and ESPSS calculations and corresponding nozzle shape change.

shape change on the erosion rate distribution can be more easily appreciated. All ESPSS models show a similar modification of the erosion distribution passing from the initial to the final time instant, with an increased erosion in the convergent and divergent zones relatively to the throat one. A similar behavior is obtained from the ablative CFD simulations.

Results in terms of nozzle shape change according to the ESPSS libraries shows how both nozzle erosion models considered perform qualitatively well along the nozzle length with respect to experimental and CFD data (see Figure 12). In particular, results obtained with the FRchem model are almost overlapped to the CFD one. On the other hand, the semi-empirical correlation model slightly underestimate the CFD results.

4.4 Nozzle erosion of hybrid rocket engines validation

The first test campaign analyzed for the nozzle erosion models validation in HRE environment employs HDPE as the fuel and LOX as the oxidizer [38]. A selection of three tests has been considered for the validation (see Table 8), ranging from extremely fuel-rich conditions (i.e., test B-7) to oxidizer-rich conditions (i.e., test A-5). In this way, the capability of the ESPSS ablation models in dealing with different flow conditions in terms of equivalence ratio can be assessed. Two nozzle erosion models have been used in the simulations: the semi-empirical correlation for HRE and the FRchem model.

In Figure 13, results in terms of throat erosion rate and wall temperature are summarized for the three test conditions in Table 8. Concerning throat erosion rates (see Figure 13a), ESPSS models shows a good capability of

DOI: 10.13009/EUCASS2022-6165

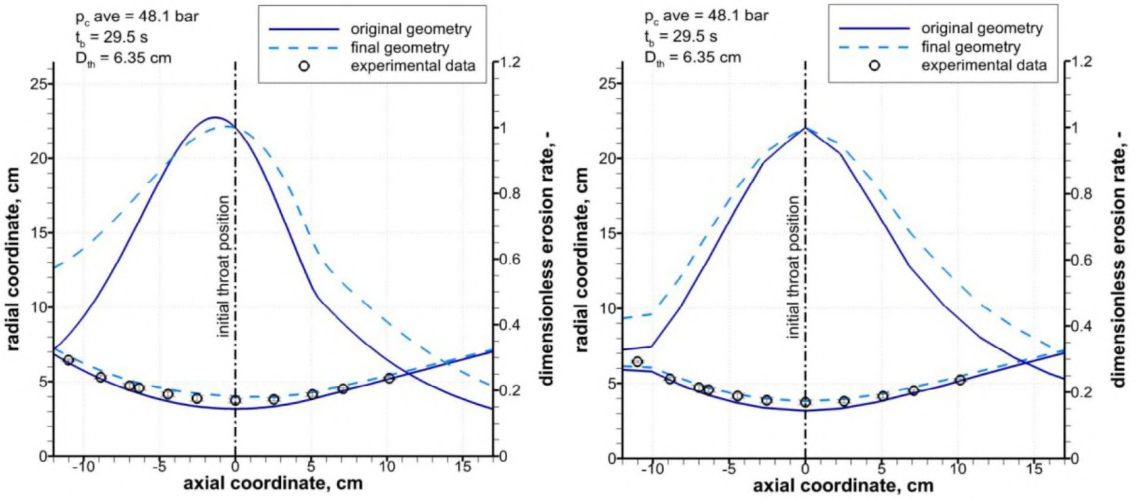

(a) CFD.

(b) ESPSS – semi-empirical.

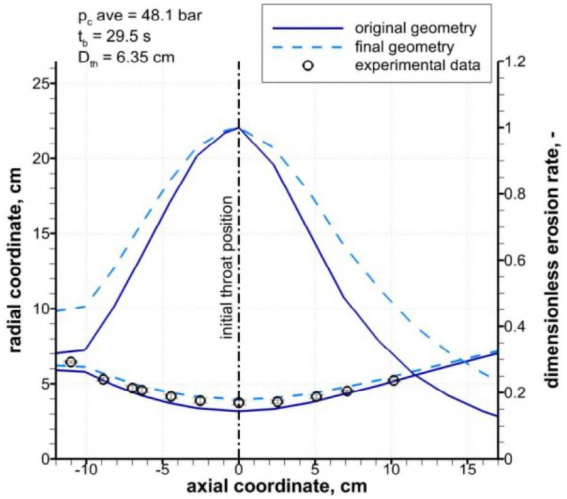

(c) ESPSS–FRchem model.

Figure 11: Dimensionless erosion rate distributions along the nozzle length at the initial (0.2 s) and final (28 s) times according to CFD and ESPSS computations.

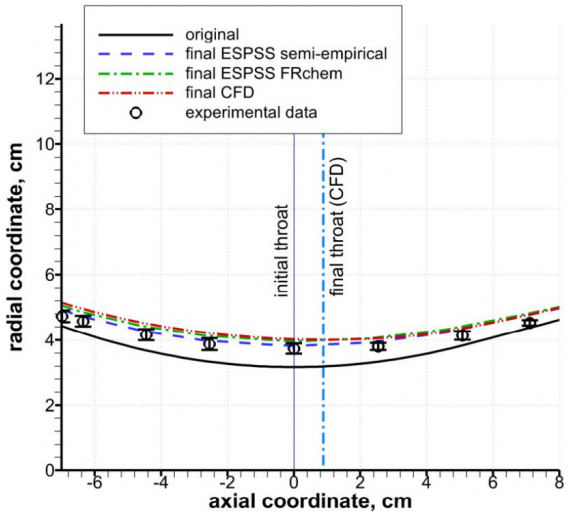

Figure 12: Hippo motor shape change according to ESPSS nozzle erosion models and CFD simulations and comparison with the experimental data.

DOI: 10.13009/EUCASS2022-6165

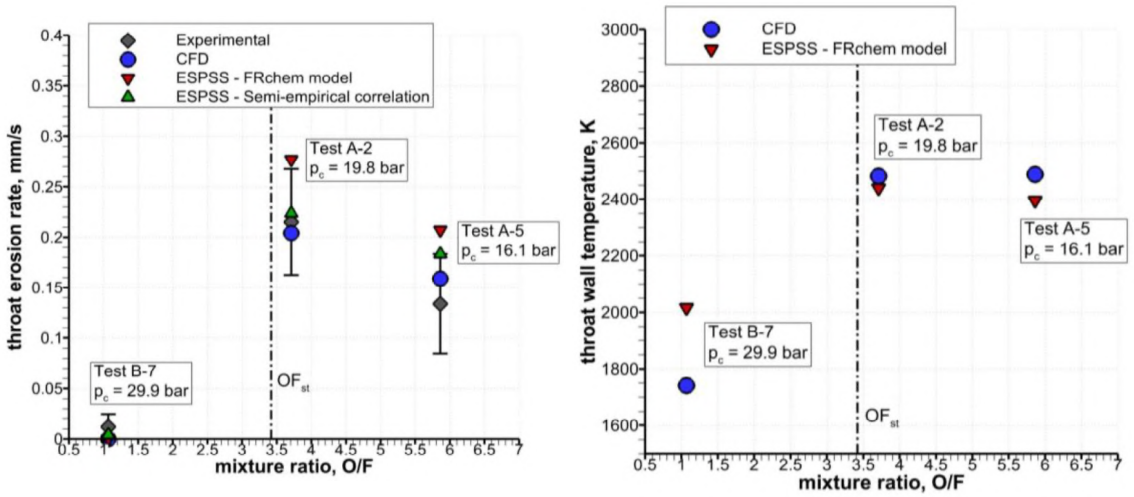

(a) Throat erosion rate.

(b) Throat wall temperature.

Figure 13: Throat erosion rate and wall temperature obtained from ESPSS for the HDPE/LOX tests (see Table 8) and comparison with experimental data and CFD computations.

reproducing the ablative behavior at varying oxidizer-to-fuel mass ratio. In particular, for test B-7 (i.e., fuel-rich conditions), an almost null throat erosion has been computed with all the ESPSS models tested, even if chamber pressure is quite high. Experimental evidences and CFD data confirm this result. Instead, looking to near stoichiometric conditions (i.e., Test A-2), an high throat erosion rate has been obtained. The empirical correlation result is almost superimposed to the experimental and CFD data, while the FRchem model slightly overestimates them, even if remaining significantly close to the experimental uncertainty bar. The considerations made for Test A-2 applies for Test A-5 as well (i.e., oxidizer-rich conditions). On the other side, concerning throat wall temperature (see Figure 13b), ESPSS results are quite in line with CFD data, except for Test B-7, for which a +14.5% overestimation is observed.

In conclusion, qualitative variations of both throat erosion rate and wall temperature at varying oxidizer-to-fuel mass ratio and chamber pressure in HRE are successfully captured by the ESPSS erosion models employing oxygen as the oxidizer.

The second test campaign analyzed for the nozzle erosion models validation in HRE environment employs HDPE as the fuel and N2O (i.e., nitrous oxide) as the oxidizer [39]. A selection of three tests has been considered for the validation (see Table 9), consisting in a fuel rich test case (Test C-3), and two near stoichiometric test cases (Test C-1 and C-2). Only the FRchem model has been used, as the semi-empirical correlation for HRE is valid only if oxygen is used as the oxidizer.

In Figure 14, results in terms of throat erosion rate and wall temperature are summarized for all the three test conditions in Table 9. Concerning throat erosion rates (see Figure 14a), the ESPSS FRchem model appears to well reproduce the ablation behavior at varying oxidizer-to-fuel mass ratio. In particular, results are always inside the experimental uncertainty bar. On the other side, concerning throat wall temperature (see Figure 14b), ESPSS results are quite in line with experimental and CFD data for all the test cases analyzed.

Therefore, it can be stated that the qualitative variations of both throat erosion rate and wall temperature at varying oxidizer-to-fuel mass ratio and chamber pressure are successfully captured. In particular, this confirms the significantly flexible applicability of the FRchem model, which is the only nozzle erosion model included in the ESPSS libraries which can be used for both SRM and HRE applications, and without any limitation in terms of propellant combination and/or composition.

5. Conclusions

An extensive literature review allowed to gather and select the most suitable low-order models, both for chamber film cooling in liquid rockets and for nozzle erosion in solid and hybrid rockets, to be implemented in the ESPSS libraries. These models are capable of providing different accuracy-to-computational burden ratios, required by the ESPSS scope and architecture. After a brief presentation of the formulations, this study aimed at the validation of those models, and at assessing their predictive capabilities. All the models have been validated by comparison among ESPSS results,

DOI: 10.13009/EUCASS2022-6165

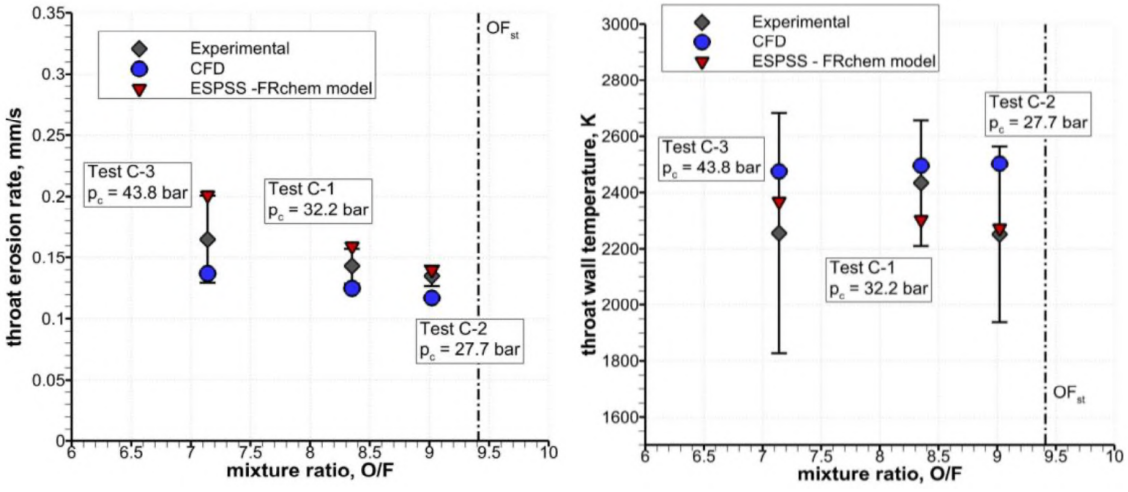

(a) Throat erosion rate.

(b) Throat wall temperature.

Figure 14: Throat erosion rate and wall temperature obtained from ESPSS for the HDPE/N2O tests (see Table 9) and comparison with experimental data and CFD computations.

experimental data, and CFD computations.

Two brand new ESPSS components have been developed to include the film cooling models, while the implementation of the nozzle erosion models has been carried out within the original ESPSS solid/hybrid thrust chamber super-components, without altering in any significant way their original architecture.

Three liquid film cooling models with different level of detail have been validated against the few experimental data found in the literature. All of them have shown low error ranges on thrust and characteristic velocity (∼5%), indicating a correct evaluation of the performance losses due to the cold film injection. Higher but still acceptable errors (∼15%) have been obtained on the film cooled length, depending in particular on the level of approximation characterizing each model. Unfortunately, such error on the film length propagates in the estimate of the wall heat flux, where it can reach higher values up to ∼30-35% depending on the operating conditions. Moreover, only one model, namely the complete Grisson model, is capable of providing that reasonable estimate of the heat flux. Despite a more detailed and comprehensive treatment should be used to have insights into the complex phenomenology occurring in a liquid film cooled combustion chamber, such as film breakup, atomization, entrainment, etc, leading to heavy computational burdens, the present low-order approaches have shown to meet a reasonable agreement with the experimental data.

Concerning gaseous film cooling, the model by Di Matteo has been selected, improved and validated against oxygen/hydrogen and oxygen/methane applications. Similar results have been obtained in the two cases, with errors not exceeding 20% on the total wall heat flux along the combustion chamber. Discrepancies are comparable with those obtained by more complex and detailed CFD simulation, under different operating conditions, confirming the reasonable heat load prediction capability of low-order models, in case of gaseous film cooling.

Four different models have been implemented, two for SRMs and two for HREs, employing different levels of accuracy. In particular, two zero-dimensional semi-empirical correlations, the B' tables model and a finite rate chemical kinetics model have been implemented.

Concerning SRM applications, three different test campaigns have been investigated. In the analysis of the ISPM motor test campaign it has been underlined how the equilibrium B' tables model cannot be used in case of non-metallized solid propellants, as in this case ablation is kinetic-limited. The BATES motor test campaign allowed for the validation of all the models implemented for metallized solid propellants. Moreover, it has been underlined how the equilibrium B' model leads to more and more reliable results as the solid grain aluminum content is increased due to the establishment of a diffusion-limited ablation regime. The analysis of the Hippo motor allows for the validation of the full-nozzle shape change capabilities included in the nozzle erosion models implemented. The nozzle geometry time evolution and the associated shape change effects on the nozzle erosion rate distribution in time have been correctly predicted by ESPSS computations.

On the other side, concerning HRE applications, two different test campaigns have been analyzed (i.e., HDPE/LOX and HDPE/N2O tests). In both cases, the models employed have shown to be able to reproduce the expected ablation behavior at varying chamber pressure and, most important, at varying oxidizer-to-fuel mass ratio. In fact, throttling and

DOI: 10.13009/EUCASS2022-6165

mixture ratio shift are a peculiar characteristic of HRE, altering the ablation process. In particular, all the models are able to correctly predict an almost null erosion (even in case of quite high chamber pressures) when strongly fuel-rich conditions are encountered, while providing higher erosion rates at near-stoichiometric and oxidizer-rich conditions.

Acknowledgments

This research has been supported by European Space Agency (ESA), within the frame of Contract No. 4000129564/-19/NL/MG. The authors acknowledge the support of Fernando R Lucas and María Aranda Rosales of Empresarios Agrupados Internacional in the software integration procedure into the ESPSS libraries.

References

[1] Eldon L Knuth. *The mechanics of film cooling*. PhD thesis, California Institute of Technology, 1954.

[2] L Crocco. An approximate theory of porous, sweat, or film cooling with reactive fluids. *Journal of the American Rocket Society*, 22(6):331–338, 1952.

[3] Alfred R Graham. *Film cooling of rocket motors*. PhD thesis, Jet Propulsion Center, Purdue University, 1958.

[4] John Paul Sellers. Experimental and theoretical study of the application of film-cooling to a cylindrical rocket thrust chamber. 1958.

[5] RA Gater, MR L'Ecuyer, and CF Warner. Liquid-film cooling, its physical nature and theoretical analysis. Technical report, Purdue university Lafayette in jet propulsion center, 1965.

[6] Pravin Sawant, Mamoru Ishii, and Michitsugu Mori. Droplet entrainment correlation in vertical upward co-current annular two-phase flow. *Nuclear Engineering and Design*, 238(6):1342–1352, 2008.

[7] EB Coy, SA Schumaker, and MA Lightfoot. Film cooling of liquid hydrocarbon engines for operationally-responsive space access. Technical report, AIR FORCE RESEARCH LAB EDWARDS AFB CA PROPULSION DIRECTORATE, 2010.

[8] RL Ewen and HM Evensen. *Liquid Rocket Engine Self-cooled Combustion Chambers: NASA Space Vehicle Design Criteria (chemical Propulsion)*. National Aeronautics and Space Administration, 1977.

[9] William M Grisson. Liquid film cooling in rocket engines. Technical report, Morehouse Coll Atlanta GA, 1991.

[10] SR Shine, S Sunil Kumar, and BN Suresh. A new generalised model for liquid film cooling in rocket combustion chambers. *International Journal of Heat and Mass Transfer*, 55(19-20):5065–5075, 2012.

[11] RA Seban, HW Chan, and S Scesa. *Heat transfer to a turbulent boundary layer downstream of an injection slot*. American Society of Mechanical Engineers, 1957.

[12] SC Kacker and James H Whitelaw. The effect of slot height and slot-turbulence intensity on the effectiveness of the uniform density, two-dimensional wall jet. 1968.

[13] Kiran H Dellimore, Andre W Marshall, and Christopher P Cadou. Influence of compressibility on film-cooling performance. *Journal of Thermophysics and Heat Transfer*, 24(3):506–515, 2010.

[14] Richard J Goldstein. Film cooling. In *Advances in heat transfer*, volume 7, pages 321–379. Elsevier, 1971.

[15] RJ Goldstein and A Haji-Sheikh. Prediction of film cooling effectiveness. In *Proceedings of Japanese Society of Mechanical Engineers, Semi-International Symposium*, volume 2, page 213, 1967.

[16] Richard Arnold, Dmitry Suslov, and OJ Haidn. Film cooling of accelerated flow in a subscale combustion chamber. *Journal of propulsion and power*, 25(2):443–451, 2009.

[17] Frederick F Simon. Jet model for slot film cooling with effect of free-stream and coolant turbulence. *NASA STI/Recon Technical Report N*, 87:18034, 1986.

[18] Francesco Di Matteo, Matteo Venanzi, Marco De Rosa, and Marcello Onofri. Modelling and simulation of film cooling in liquid rocket engine propulsion systems. page 3908, 2012.

DOI: 10.13009/EUCASS2022-6165

[19] R Kendall, R Rindal, C Moyer, and E Bartlett. User's manual: Aerotherm charring material thermal response and ablation program - version 3. Technical Report AD875062, AFRPL, 1970.

[20] J. Lachaud, Thierry E Magin, Ioana Cozmuta, and N.N. Mansour. A short review of ablative-material response models and simulation tools. In *7th aerothermodynamics symposium, ESA*, 2011.

[21] Peter G. Cross and Iain D. Boyd. Two-dimensional modeling of ablation and pyrolysis with application to rocket nozzles. *Journal of Spacecraft and Rockets*, 54(1):212–224, 2017.

[22] K. K. KUO and S. T. KESWANI. A comprehensive theoretical model for carbon-carbon composite nozzle recession. *Combustion Science and Technology*, 42(3-4):145–164, 1985.

[23] S. T. KESWANI and K. K. KUO. Validation of an aerothermochemical model for graphite nozzle recession and heat-transfer processes. *Combustion Science and Technology*, 47(3-4):177–192, 1986.

[24] Piyush Thakre and Vigor Yang. Chemical erosion of carbon-carbon/graphite nozzles in solid-propellant rocket motors. *Journal of Propulsion and Power*, 24(4):822–833, 2008.

[25] Daniele Bianchi, Francesco Nasuti, and Emanuele Martelli. Coupled analysis of flow and surface ablation in carbon-carbon rocket nozzles. *Journal of Spacecraft and Rockets*, 46(3):492–500, 2009.

[26] Daniele Bianchi, Francesco Nasuti, Marcello Onofri, and Emanuele Martelli. Thermochemical erosion analysis for graphite/carbon-carbon rocket nozzles. *Journal of Propulsion and Power*, 27(1):197–205, 2011.

[27] Daniele Bianchi and Francesco Nasuti. Carbon-carbon nozzle erosion and shape-change effects in full-scale solid-rocket motors. *Journal of Propulsion and Power*, 28(4):820–830, 2012.

[28] A. Turchi, D. Bianchi, P. Thakre, F. Nasuti, and V. Yang. Radiation and roughness effects on nozzle thermochemical erosion in solid rocket motors. *Journal of Propulsion and Power*, 30(2):314–324, 2014.

[29] Daniele Bianchi and Francesco Nasuti. Numerical analysis of nozzle material thermochemical erosion in hybrid rocket engines. *Journal of Propulsion and Power*, 29(3):547–558, 2013.

[30] Daniele Bianchi, Alessandro Turchi, Francesco Nasuti, and Marcello Onofri. Chemical erosion of carbon-phenolic rocket nozzles with finite-rate surface chemistry. *Journal of Propulsion and Power*, 29(5):1220–1230, 2013.

[31] Daniele Bianchi and Francesco Nasuti. Navier–stokes simulation of graphite nozzle erosion at different pressure conditions. *AIAA Journal*, 53(2):356–366, 2015.

[32] Daniele Bianchi, Landon T. Kamps, Francesco Nasuti, and Harunori Nagata. Numerical and experimental investigation of nozzle thermochemical erosion in hybrid rockets. In *AIAA*, paper 2017-4640 ,2017.

[33] Daniele Bianchi and Agostino Neri. Numerical simulation of chemical erosion in vega solid-rocket-motor nozzles. *Journal of Propulsion and Power*, 34(2):482–498, 2018.

[34] Daniele Bianchi, Mario Tindaro Migliorino, Francesco Nasuti, and Marcello Onofri. *CFD Analysis of Paraffin-Based Hybrid Rockets with Coupled Nozzle Erosion Characterization*. AIAA paper 2019-4263, 2019.

[35] D. Baer and A. Ambrosio. Heat conduction in a semi-infinite slab with sublimation at the surface. *Planetary and Space Science*, 4:436 – 446, 1961.

[36] R. Geisler and C. Beckman. The history of the bates motors at the air force rocket propulsion laboratory. In *34th AIAA/ASME/SAE/ASEE Joint Propulsion Conference and Exhibit*, 1998.

[37] Enrico Cavallini, Daniele Bianchi, Bernardo Favini, Maurizio Di Giacinto, and Ferruccio Serraglia. Internal ballistics modeling of high performance srms with coupled nozzle erosion characterization. In *47th AIAA/ASME/SAE/ASEE Joint Propulsion Conference & Exhibit*, paper 2011-5799, 2012.

[38] Daniele Bianchi, Mario Tindaro Migliorino, Marco Rotondi, Landon Kamps, and Harunori Nagata. Numerical analysis of nozzle erosion in hybrid rockets and comparison with experiments. *Journal of Propulsion and Power*, pages 1–22, 2021. Articles in advance.

[39] Marco Rotondi, Mario Tindaro Migliorino, Daniele Bianchi, Landon T. Kamps, and Harunori Nagata. Numerical analysis of nozzle transient heating and erosion in hybrid rockets burning hdpe. In *AIAA*, paper 2021-3496, 2021.

DOI: 10.13009/EUCASS2022-6165

[40] E. P. Bartlett, R. M. Kendall, and R. A. Rindal. Thermochemical ablation. In *AIAA*, paper 65-642, 1965.

[41] L. Lees. Convective heat transfer with mass addition and chemical reactions. In *Third AGARD Colloquim on Combustion and Propulsion*, 1959.

[42] F. Untem, F. Calciolari, L. de Almeida, G. Murari, and W. A. Silva. A fast method for preliminary evaluation of chemical erosion on a composite nozzle. In *4th Brazilian Conference on Composite Materials*, 2018.

[43] J. Vilà, J. Moral, V. Fernández-Villacé, and Steelant J. An overview of the espss libraries: Latest developments and future. In *Space Propulsion Conference*, 2018.

[44] B Leckner. Spectral and total emissivity of water vapor and carbon dioxide. *Combustion and flame*, 19(1):33–48, 1972.

[45] Gianluca Sdoga. *Tecnica del film cooling in endoreattori a propellente liquido: sviluppo e validazione di un modello empirico mediante simulazioni CFD*. M.sc. dissertation, Sapienza University of Rome, 2020.

[46] J. Moral, F. Rodriguez, J. Vilà, F. Di Matteo, and Steelant J. 1-d simulation of solid and hybrid combustors with ecosimpro/espss. In *Space Propulsion Conference*, 2014.

[47] Technical notes: A simple equation for rapid estimation of rocket nozzle convective heat transfer coefficients. *Journal of Jet Propulsion*, 27(1):49–53, 1957.

[48] S. Gordon and B. J. McBride. Computer program for calculation of complex chemical equilibrium compositions and applications. Technical Report RP-1311, NASA, 1994.

[49] D.R. Bartz. Turbulent boundary-layer heat transfer from rapidly accelerating flow of rocket combustion gases and of heated air. *Advances in Heat Transfer*, 2:1–108, 1965.

[50] D. Bradley, G. Dixon-Lewis, S. El din Habik, and E.M.J. Mushi. The oxidation of graphite powder in flame reaction zones. *Symposium (International) on Combustion*, 20(1):931 – 940, 1985.

[51] Gerald Morrell. Investigation of internal film cooling of 1000-pound-thrust liquid-ammonia-liquid-oxygen rocket-engine combustion chamber. 1951.

[52] Jong-Gyu Kim, Kwang-Jin Lee, Seonghyeon Seo, Yeoung-Min Han, Hong-Jip Kim, and Hwan-Seok Choi. Film cooling effects on wall heat flux of a liquid propellant combustion chamber. In *42nd AIAA/ASME/SAE/ASEE Joint Propulsion Conference & Exhibit*, page 5196, 2006.

[53] Richard Arnold, Dmitry I Suslov, and OJ Haidn. Film cooling in a high-pressure subscale combustion chamber. *Journal of propulsion and power*, 26(3):428–438, 2010.

[54] Dmitry Suslov, B Betti, T Aichner, S Soller, F Nasuti, and O Haidn. Experimental investigation and cfd-simulation of the film cooling in an o2/ch4 subscale combustion chamber. In *Space Propulsion Conference*. Association Aéronautique et Astronautique de France Paris, France, 2012.

[55] Brian J. Evans. *Nozzle erosion characterization and minimization for high-pressure rocket motor applications*. PhD thesis, 2010.

[56] R. GEISLER, C. BECKMAN, and S. KINKEAD. The relationship between solid propellant formulation variables and motor performance. In *AIAA 11th Propulsion Conference*, 1975.

[57] J. Arnold, J. Dodson, and B. Laub. Subscale solid motor nozzle tests (phase iv), and nozzle materials screening and thermal characterization (phase v). Technical Report CR 161254, NASA, 1979.

[58] Barbara Betti, Emanuele Martelli, Francesco Nasuti, and Marcello Onofri. Numerical study of heat transfer in film cooled thrust chambers. In *48th AIAA/ASME/SAE/ASEE Joint Propulsion Conference & Exhibit*, page 3907, 2012.